nature nanotechnology

ARTICLES

https://doi.org/10.1038/s41565-022-01197-y

# Metasurface optofluidics for dynamic control of light fields

Qitong Li[1], Jorik van de Groep[1,2], Adam K. White[3], Jung-Hwan Song[1], Scott A. Longwell[3], Polly M. Fordyce[3,4,5,6], Stephen R. Quake[3,6,7], Pieter G. Kik[1,8] and Mark L. Brongersma[1] ✉

**The ability to manipulate light and liquids on integrated optofluidics chips has spurred a myriad of important developments in biology, medicine, chemistry and display technologies. Here we show how the convergence of optofluidics and metasurface optics can lead to conceptually new platforms for the dynamic control of light fields. We first demonstrate metasurface building blocks that display an extreme sensitivity in their scattering properties to their dielectric environment. These blocks are then used to create metasurface-based flat optics inside microfluidic channels where liquids with different refractive indices can be directed to manipulate their optical behaviour. We demonstrate the intensity and spectral tuning of metasurface colour pixels as well as on-demand optical elements. We finally demonstrate automated control in an integrated meta-optofluidic platform to open up new display functions. Combined with large-scale microfluidic integration, our dynamic-metasurface flat-optics platform could open up the possibility of dynamic display, imaging, holography and sensing applications.**

Microfluidics facilitates highly automated direction, mixing and manipulation of minute volumes of liquids[1] and has been instrumental in advancing a wide variety of technologies that range from culturing cells and high-throughput diagnostics in biology[2,3] to microreactors for synthetic chemistry[4]. The tremendous synergy derived from integrating optics and fluidics on a single chip has further expanded the possibilities as liquids can be used to control local optical properties, and conversely, light can also be used to monitor chemical and biological processes inside liquids[5–8]. Initial attempts have been made to extend this integration to metasurface-based flat optics[9] in gigahertz[10] and terahertz[11] regimes. Here we apply different materials and a conceptually new mechanism to move this integration to the very important visible spectral range and provide new optical functions that can be transformative in the development of novel displays, dynamic on-demand flat optics and sensing technologies.

Displays are omnipresent in our daily lives as they are used in our smartphones, tablets, computer screens, televisions and data projectors. Advances in display technology may ultimately enable us to turn our entire environment, clothing and belongings into displays to personalize our life and to satisfy our ever-increasing need for information[12]. Organic light-emitting diode and liquid-crystal displays currently dominate the display market[13]. Such displays provide vivid images, but compared with regular ink on paper, there are also some important shortcomings. Paper is low cost, superior in terms of readability and does not actively consume power to display colours. Its excellent readability is the most obvious in bright daylight where liquid-crystal display and organic light-emitting diode displays exhibit unwanted glare, and the use of polarizers and colour filters limits the display's brightness. Pioneering realizations of electronic-paper displays employed the physics of electrophoresis[14] and electrowetting[15,16] in a microfluidic architecture to reversibly cover back reflectors with coloured inks, leading to widespread use of electronic-paper displays that mimic the appearance of printed papers and magazines. These displays operate at impressively low power and achieve video speeds[17]. However, the use of inks prevents long-term durability and their functionality is severely constrained to a basic light absorption function. It also remains challenging to manipulate the dimensions of ink-display pixels down to sub-micrometre resolution. Additionally, an opaque back reflector is needed to enhance reflectivity and hide idle ink underneath, hindering the realization of transparent displays. Here we illustrate why metasurfaces comprising dense arrays of strongly scattering nanostructures could become the new 'ink' by solving a number of outstanding challenges that have plagued ink displays. We demonstrate subwavelength-resolution pixels that offer bright structural colours[18–22] and long-term stability, and present new ways to dynamically control the light field[23–25]. These features can enable the realization of transparent displays and dynamic on-demand flat optics, and bring new sensing modalities. The recent demonstration that metasurfaces can increase the brightness and pixel density of organic light-emitting diode displays highlights their potential commercial use[26].

Given the virtually immutable optical properties of metals and semiconductors, it has been challenging to create dynamically tunable metasurfaces. However, the sensitivity of the optical properties of nanostructures to their dielectric environment can be harnessed to tune their scattering behaviour and colour[18,27]. Optical metasurfaces have an open structure with many voids and crevasses between the scattering nanostructures that allow easy infiltration with liquids. This made it possible to create tunable metasurfaces using mature liquid-crystal technology[28–31]. Here we demonstrate a meta-optofluidic platform on a transparent substrate capable of dynamic intensity and spectral control of light fields without the need for polarizers or colour filters.

---

[1]Geballe Laboratory for Advanced Materials, Stanford University, Stanford, CA, USA. [2]Van der Waals–Zeeman Institute for Experimental Physics, Institute of Physics, University of Amsterdam, Amsterdam, Netherlands. [3]Department of Bioengineering, Stanford University, Stanford, CA, USA. [4]Department of Genetics, Stanford University, Stanford, CA, USA. [5]ChEM-H Institute, Stanford University, Stanford, CA, USA. [6]Chan Zuckerberg Biohub, San Francisco, CA, USA. [7]Department of Applied Physics, Stanford University, Stanford, CA, USA. [8]CREOL, The College of Optics and Photonics, University of Central Florida, Orlando, FL, USA. ✉e-mail: brongersma@stanford.edu

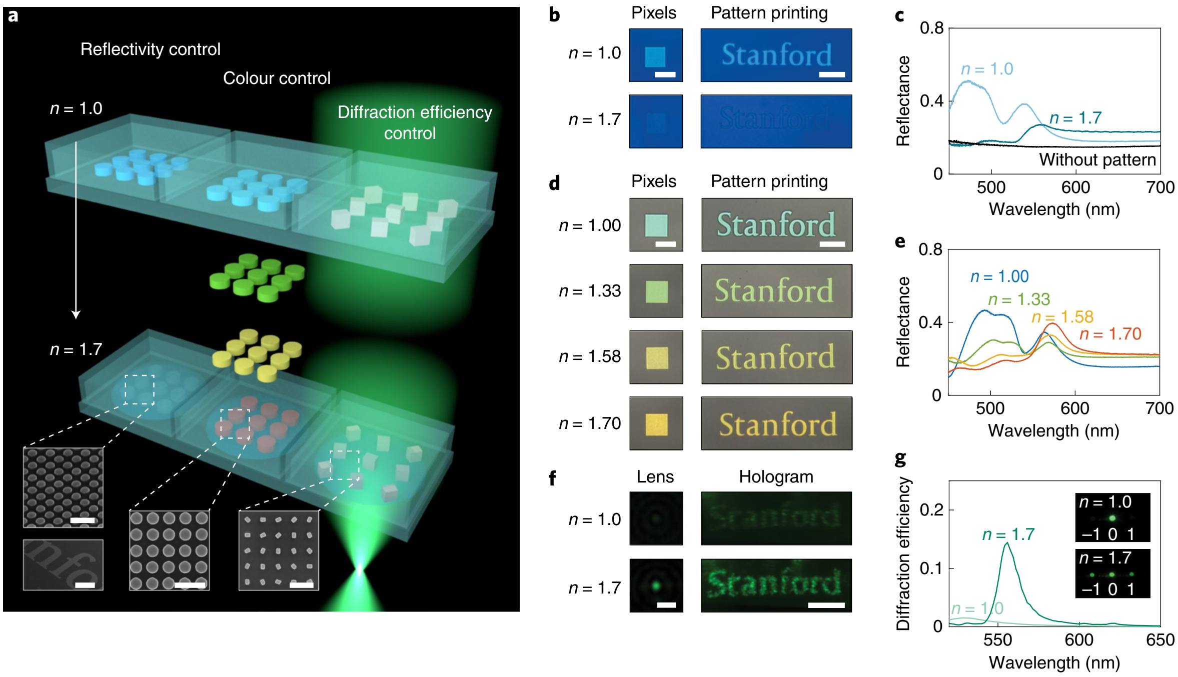

**Fig. 1 | A comprehensive dynamic-metasurface optofluidic platform. a**, Schematic of three Si metasurfaces with different dynamic control functions fabricated on the same chip. Integrated microfluidics provide on-demand control over the refractive index ($n = 1.0$–$1.7$) of the environment of nanoresonators in a metasurface by flowing liquids with different refractive indices in real time. Inset: scanning electron microscopy (SEM) images of the fabricated metasurfaces that provide the corresponding functions. Scale bars, 10 μm (bottom-left SEM image); 500 nm (all other SEM images). **b**,**c**, Reflection optical images (**b**) and measured reflection spectra (**c**) of the metasurfaces (height, $h = 75$ nm; diameter, $D = 165$ nm; period, $p = 250$ nm) for dynamic reflectivity tuning. A 530 nm short-pass colour filter is inserted to enhance the contrast in **b**. Scale bars, 25 μm. **d**,**e**, Reflection optical images (**d**) and measured reflection spectra (**e**) of the metasurfaces ($h = 75$ nm, $D = 185$ nm, $p = 280$ nm) for dynamic colour tuning. Scale bars, 25 μm. **f**, Optical images of the back focal plane of a meta-lens (NA = 0.45) (left) and far-field distribution of a meta-hologram (right) illustrating the dynamic diffraction efficiency tuning of optics on demand. Scale bars, 3 μm (left), 1 mm (right). **g**, Measured diffraction efficiency spectra of geometric phase metasurfaces ($h = 120$ nm; length, $L = 120$ nm; width, $W = 90$ nm; $p = 320$ nm). Insets: the Fourier plane of a meta-grating that can effectively steer the beam when turned on.

## Development of a dynamic-metasurface optofluidic platform

Figure 1a visualizes several important dynamic control functions that can be achieved by incorporating silicon (Si) metasurfaces inside a microfluidic channel. The nanostructures are designed to alter their scattering properties in real time by flowing liquids over them with different refractive indices ($n = 1.0$–$1.7$) (Supplementary Fig. 1 shows the numerical simulations of dynamic functions). First, we experimentally demonstrate the dynamic reflectivity tuning of colour pixels (Supplementary Fig. 8 shows the experimental geometries). We employ a square lattice of Si nanodisks to ensure a polarization-independent response. Although the geometry of colour pixels in conventional ink displays is defined by the shape of tiny liquid cells, the metasurface colour pixels can be patterned in arbitrary shapes and offer diffraction-limited resolution. Figure 1b shows the highly reflective 'on' state of a single, blue pixel and various characters for a channel filled with air ($n = 1.0$) and the low-reflectivity 'off' state that results from flowing a liquid with $n = 1.7$. The $25 \times 25\,\mu m^2$ metasurface pixel contains 10,000 Si nanodisks and yet appears optically uniform due to the subwavelength disk spacing. The printed word 'Stanford' highlights the sub-micrometre resolution enabled by metasurface 'inks'. The switching of pixels requires large and broadband changes in reflectivity, as evident in our spectral measurements (Fig. 1c). Second, we demonstrate the dynamic colour tuning of reflective pixels with another metasurface design. In both optical reflection images (Fig. 1d) and measured reflection spectra (Fig. 1e), we observe the gradual tuning of colour across the visible spectrum as the index in the channel increases from 1.0 to 1.7. Third, we show how we can realize optics on demand, where optical elements can be made to appear and disappear. This requires efficient, dynamic control over the diffraction efficiency of phased-array optics. To illustrate this concept, we design and fabricate a geometric phase metasurface[32] composed of rotated rectangular Si nanoblocks that encodes a local geometric phase profile with subwavelength resolution. This creates an engineered wavefront that generates a desired light-field distribution. These metasurfaces can be designed to encode various functions, such as high-numerical-aperture (NA) beam focusing, holography (Fig. 1f) and large-angle beam steering (Fig. 1g, insets). Figure 1g shows that these optical functions are initially turned off in the entire visible-frequency range when $n = 1.0$. They can be gradually turned on as we increase the refractive index of the surrounding medium. We quantitatively measure the increase in intensity from 0.6% to 14.4% of the incident intensity at 555 nm, a 24-fold increase in the diffraction efficiency.

## Modelling metasurfaces with tunable fictitious surface currents

To achieve the abovementioned functions, we capitalize on the presence and strong dispersion of several optical resonances that are supported by the Si nanodisk arrays in the visible spectral range. Previous research on the Kerker effect[33–35] has shown that the resonant multipolar excitation of nanostructures can be used to very effectively direct the flow of light. The far-field scattering for each multipole is characterized by a unique angular distribution and phase symmetry. When two or more multipoles are simultaneously excited, strong interference effects can be observed and harnessed to direct the scattered light.

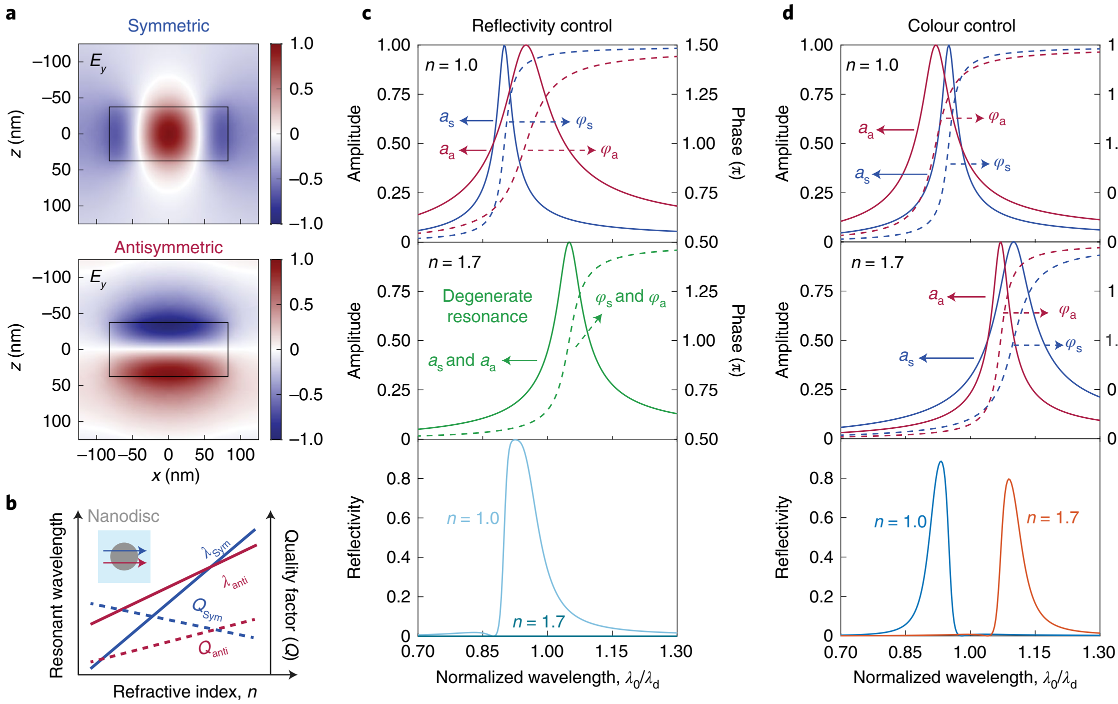

**Fig. 2 | Mechanism of dynamic reflectivity and colour control in Si metasurfaces. a**, Electric-field distributions ($E_y$) of two dominant optical resonances in a Si nanodisk array with symmetric and antisymmetric radiation profiles. **b**, Illustration of two dominant optical resonances in nanodisks showing different dispersions with the refractive index of the surrounding medium. Inset: the top view of a unit cell of a nanodisk array supporting two dominant optical resonances. **c**, Analysis for dynamic reflectivity control by Si metasurfaces. The top and middle panels show the amplitude ($a$, solid lines) and phase ($\varphi$, dashed lines) of the scattered plane waves from the symmetric (blue) and antisymmetric (red) modes as a function of the incident wavelength when the Si metasurface is embedded in different dielectric environments ($n=1.0$ (1.7) for the top (middle) panel). The bottom panel shows the calculated reflection spectra of the metasurface for dynamic reflectivity control. **d**, Similar analysis to **c** but for dynamic colour control. The designed wavelength $\lambda_d$ is set as 550 nm.

This line of thinking has led to the design of Huygens' metasurfaces comprising many Kerker scatterers[36–38]. Here we design highly tunable metasurfaces by expanding on these notions and applying them to dispersive resonators. Specifically, we engineer the nanostructures to display different spectral shifts and changes in their quality factors when the local index is altered. We show that this ability to dynamically move and shape the optical resonances offers a valuable new route to control the flow of light in a spectrally dependent manner.

The scattering properties of metasurface elements can be modelled by fictitious electric ($J_s$) and magnetic ($M_s$) surface currents[36]. The magnitude of these currents can be found by summing the contributions from all the excited multipoles with a top-bottom symmetric (for $J_s$) or antisymmetric (for $M_s$) radiation phase with respect to the metasurface plane (Supplementary Note 1 and Supplementary Fig. 2). For the disk sizes and geometries considered here, we find two dominant optical resonances in the visible spectral range via a quasi-normal-mode analysis[39]. Their electric-field distributions show the required symmetric and antisymmetric phase symmetries (Fig. 2a). With increases in the refractive index of the surrounding medium, the two resonances exhibit notably different spectral shifts and changes in optical quality factor (Fig. 2b; Supplementary Fig. 3 provides details on modal dispersion). This can be attributed to the differences in the modal confinement to the nanodisks as well as the optical coupling between neighbouring disks. The latter is modified by dielectric screening when the environmental index is altered (Supplementary Note 2). We find that compared with the antisymmetric mode in which the electric field is tightly confined in the nanodisks, the electric field of the symmetric mode has three antinodes inside the disk and is more extended beyond the disk boundary. This results in a strong overlap of the near fields with the dielectric environment and therefore very effective shifting of the resonance wavelength. Therefore, the symmetric mode exhibits a stronger spectral shift than the antisymmetric mode. Meanwhile, radiative coupling is dominant for the antisymmetric mode, which can lead to a boost in the quality factor when the effective lattice constant approaches the resonant wavelength[40]. As a result, we can achieve broad tuning of the relative spectral positions and bandwidths of the two dominant optical resonances. This implies that at a fixed wavelength, the amplitude and phases of the scattered fields can greatly vary, which can be used to manipulate the reflection, transmission and absorption properties.

For our metasurface, we find that $J_s$ and $M_s$ have dominant contributions from one symmetric and one antisymmetric resonance. For this reason, many of the observed spectral features can be qualitatively understood using a temporal coupled-mode theory for two resonators with Lorentzian spectral lineshapes: one for the symmetric mode and the other for the antisymmetric mode. The model expresses the metasurface reflectivity $R$ in terms of the angular frequency $\omega$ of the incident light wave and the refractive index of the surrounding medium $n$:

$$R(n,\omega)=|r(n,\omega)|^2\cong \left|a_s(n,\omega)e^{i\varphi_s(n,\omega)}-a_a(n,\omega)e^{i\varphi_a(n,\omega)}\right|^2, \quad (1)$$

where $a_s$ ($a_a$) and $\varphi_s$ ($\varphi_a$) refer to the amplitude and phase of the plane waves emerging from the symmetric (antisymmetric) resonators, respectively. Equation (1) clearly shows how the reflectivity is controlled by the interference of these two plane waves. For this reason, the manipulation of spectral reflectivity comes down

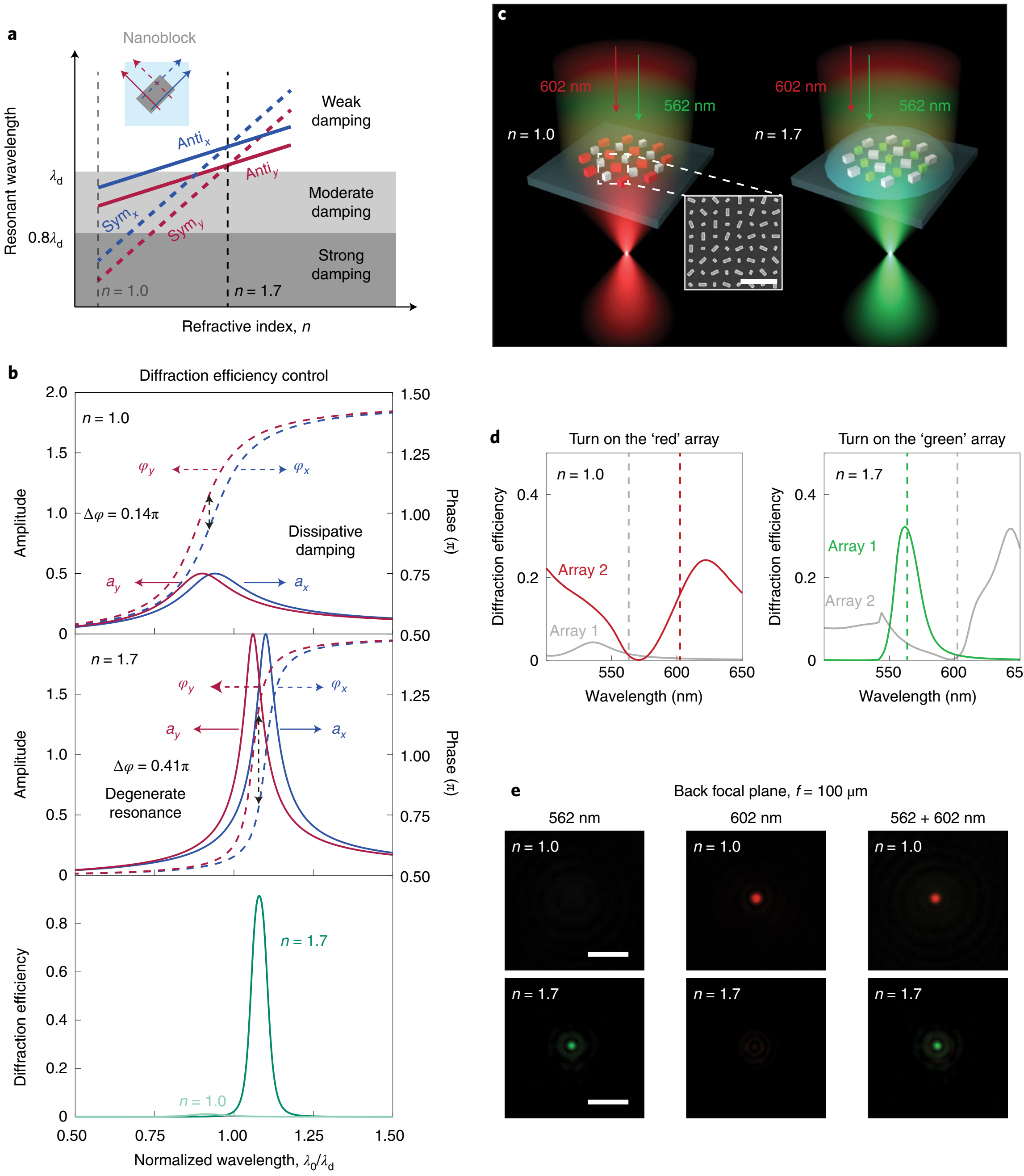

**Fig. 3 | Mechanism of dynamic diffraction efficiency control and spectral control of phased-array optics by Si geometric phase metasurfaces.** **a**, Illustration of four dominant optical resonances showing different dispersions with the refractive index of the surrounding medium. Depending on the specific resonant wavelength, certain optical resonances are damped by optical absorption in Si. Inset: the top view of a unit cell of a nanoblock array supporting the corresponding four optical resonances. **b**, The top and middle panels show the amplitude (solid lines) and phase (dashed lines) of the scattered plane waves from two anisotropic resonances for $x$ (blue) and $y$ (red) polarization as a function of the incident wavelength when the Si metasurface is embedded in different dielectric environments ($n$ = 1.0 (1.7) for the top (middle) panel). The bottom panel shows the calculated diffraction efficiency spectra of the geometric phase metasurface. The designed wavelength $\lambda_d$ is set as 550 nm. **c**, Schematic of a multiplexed meta-lens composed of two differently sized Si nanoresonator arrays that only focus red (green) light when embedded in air (high-index oil). Inset: the SEM images of the as-fabricated meta-lens. Scale bar, 1 μm. **d**, Simulated diffraction efficiency spectra for two nanoresonator arrays when the meta-lens is embedded in air (left) or high-index oil (right). **e**, Optical images of the back focal plane of the achromatic meta-lens (NA = 0.45) embedded in air (top) or high-index oil (bottom) under different illumination conditions. Scale bars, 5 μm. $f$, focal length of the meta-lens.

to achieving strong resonances (that is, large amplitudes) and controlling their relative phases. From coupled-mode theory, we find that these quantities critically depend on the resonance frequency $\omega_s$ ($\omega_a$), radiative damping $\gamma_{rs}$ ($\gamma_{ra}$) and dissipative damping $\gamma_{ds}$ ($\gamma_{da}$) of the resonators:

$$a_s(n,\,\omega)e^{i\varphi_s(n,\,\omega)} = \frac{-\gamma_{rs}(n)}{i(\omega-\omega_s(n))+\gamma_{rs}(n)+\gamma_{ds}(n)}$$

and an equivalent expression for the antisymmetric mode response. The resonator geometry, size and spacing can be engineered to

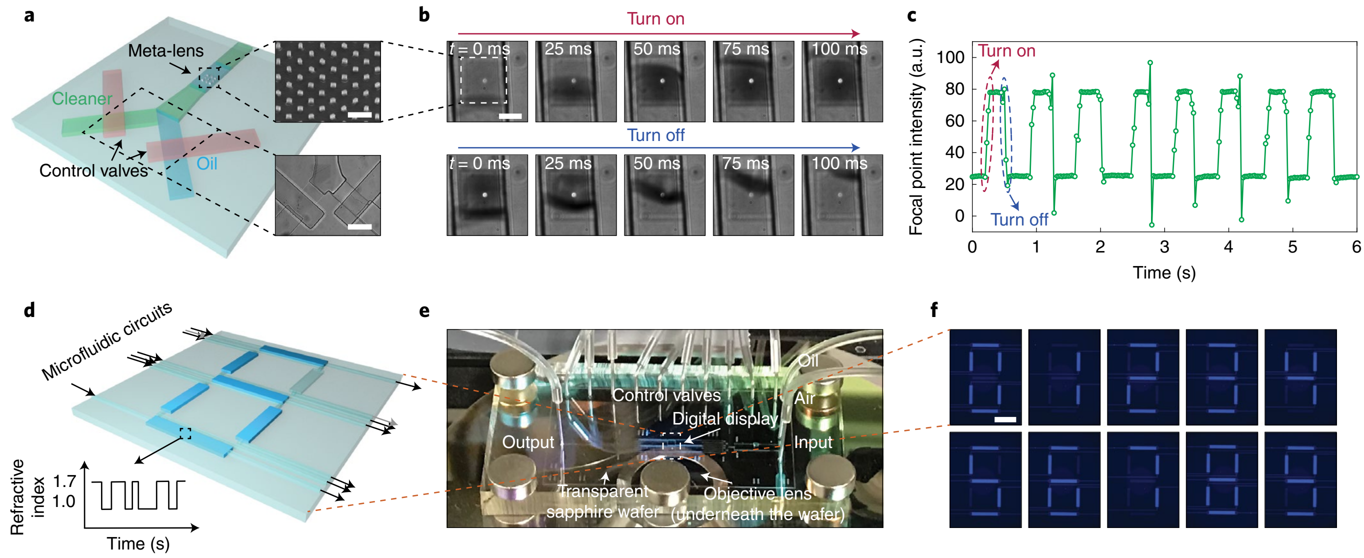

**Fig. 4 | Integration of dynamic metasurfaces with programmable microfluidics on a transparent substrate. a**, Schematic of a meta-lens (NA = 0.45) integrated with a programmable microfluidic channel. Top inset: the SEM image of the fabricated meta-lens to be integrated with the microfluidic channels. Scale bar, 500 nm. Bottom inset: the optical image of the fabricated Y-shaped microfluidic channel. Scale bar, 100 μm. **b**, A series of optical images at the back focal plane of the meta-lens taken with a time step of 25 ms to show the process of turning on (top row) and turning off (bottom row) the meta-lens. Scale bar, 50 μm. **c**, Modulated intensity in the focal point as a function of time when alternating flow of either high-index oil ($n = 1.70$) and low-index cleaner (HFE-7500, $n = 1.29$) over the meta-lens. **d**, Schematic of a transparent-metasurface digital number display controlled by programmable microfluidics. The inset shows a schematic of the real-time refractive index of the material flowing in the channel. **e**, Photograph of the integrated-metasurface digital number display. **f**, Reflection optical images of the display showing different digital numbers. Scale bar, 1 mm. The display is illuminated by unpolarized white light and a 530 nm short-pass filter is inserted to enhance the contrast.

modify these resonator properties and elicit a wide variety of effects (Fig. 1).

Equation (1) reveals that we can achieve low reflectivities when strong symmetric and antisymmetric resonances spectrally overlap. It also shows that high reflectivities are expected when these resonances are spectrally displaced such that a large (near-π) phase shift is obtained between the two resonances. Physically, this results in a situation where the currents $J_s$ and $M_s$ radiate in phase in the backwards (that is, reflection) direction. To realize dynamic reflectivity control, we capitalize on the different modal dispersions to set up a situation where the two strong resonances are spectrally displaced with environment index $n = 1.0$ and perfectly overlapped for index $n = 1.7$ (Fig. 2c). We can also achieve dynamic colour control in a system with two spectrally displaced resonances that shift to longer wavelengths together when the index is changed from $n = 1.0$ to $n = 1.7$ (Fig. 2d). Note that in this case, high reflectivities can be achieved for both refractive indices, consistent with the need for reflective displays. Quasi-normal-mode simulations are used to identify the realistic metasurface designs that can match the target modal dispersion to achieve a desired function, such as dynamic reflectivity or spectral control (Supplementary Fig. 4).

## Achieving dynamic control over on-demand optical elements

The above analysis can also be applied to understand the mechanism of dynamic diffraction efficiency control of geometric phase metasurfaces (Fig. 1d). The main difference is that geometric phase metasurfaces[41] used to achieve this type of control are constructed from anisotropic resonators (Fig. 1a). As a result, we need to account for symmetric and antisymmetric resonances that can be excited for polarization directions along the long and short axes of the resonators, resulting in four distinct resonances. The diffraction (polarization conversion) efficiency $\eta$ under circularly polarized illumination in this case becomes

$$\eta = \frac{1}{4}\left|t_x - t_y\right|^2 \cong \frac{1}{4}\left|a_x e^{i\varphi_x} - a_y e^{i\varphi_y}\right|^2, \qquad (2)$$

where $a_x e^{i\varphi_x} = a_{x,s} e^{i\varphi_{x,s}} + a_{x,a} e^{i\varphi_{x,a}}$ is the sum of the scattered plane waves from two resonators and $t_x$ is the transmission coefficient of the anisotropic resonators under $x$-polarized illumination, and an equivalent equation for $y$ polarization.

Figure 3a illustrates the dispersion of the four resonant modes with the refractive index of the surrounding medium. It is important to note that we accurately include the dissipative absorption loss in Si in these simulations. This is particularly important in this example, where the changes in amplitude and spectral width play an essential role. For $n = 1.0$, the scattering from the two symmetric resonances can be ignored as they are located in the spectral range where Si shows strong materials absorption ($\lambda < 450$ nm). The two antisymmetric modes are located at a longer wavelength ($\lambda \approx 520$ nm) and moderately damped. This results in a scattering amplitude that is halved compared with the lossless case (Fig. 3b, top). In sharp contrast, all the four resonant modes experience less material absorption and become degenerate for both polarizations when the index is changed to $n = 1.7$ and the resonances shift to $\lambda \approx 560$ nm. This results in doubling of the total scattering amplitude as well as a boost in the scattering phase difference between the two polarizations (Fig. 3b, middle). Altogether, this results in a large on/off ratio (equation (2) and Fig. 3b, bottom). This analysis corroborates the experimental result shown in Fig. 1g.

Next, we demonstrate how advanced control of modal dispersion can be leveraged to spectrally control optical functions by multiplexing two geometric phase metasurfaces composed of differently sized nanoblock arrays that resonate at different wavelengths (Fig. 3c). For example, we create a multiplexed meta-lens (NA = 0.45) capable of focusing solely red ($\lambda = 602$ nm) or green ($\lambda = 562$ nm) light on the same back focal plane, depending on the dielectric environment. Figure 3d shows the simulated diffraction efficiency spectra for two nanoresonator arrays in two different environments. The modal dispersion of each of the two types of nanoblock is judiciously engineered in such a way that both of them resonate weakly with either green or red light in the 'off' state (Fig. 3d, grey lines), but they efficiently interact with one certain colour in the 'on' state (Fig. 3d, green and red lines), driven by optical resonances at the corresponding wavelength. Figure 3e shows a series of optical images taken at the back focal plane of the meta-lens with different dielectric environments and illumination conditions, which confirm the validity of the optics-on-demand concept (Fig. 3c). We note that different phase profiles are applied for the two phased arrays, ensuring achromatic focusing.

## Integration of metasurfaces with microfluidic systems

To bring the advantages of this versatile platform closer to a practical reality, we integrate our dynamic metasurfaces with a programmable microfluidic cavity system. Such a system provides on-demand control over the refractive index ($n=1.0$–$1.7$) of the environment of the nanoresonators by flowing different liquids (or air) in real time. We first integrate a 100-µm-sized geometric phase meta-lens (NA = 0.45) with a Y-shaped microfluidic channel (Fig. 4a) to study the modulation dynamics with liquids. High-index oil ($n=1.70$) and low-index liquid cleaner (HFE-7500, $n=1.29$) are pumped into the main channel in an alternating fashion, with flow controlled by two pneumatic valves formed by crossing the control channels. This enables the modulation of intensity in the focal point by changing the liquid's refractive index. Figure 4b shows a series of optical images of the focal point as the refractive index flowing over the meta-lens is alternated between high and low to turn on and off the intensity in the focal point, respectively. The results show that the intensity modulation can be completed within 100 ms (~10 Hz). Considerable improvements in modulation speed are expected by optimizing the fabrication process of the microfluidic circuitry (Supplementary Note 3). A hydrophobic surface treatment[42,43] is also possible to help prevent the molecules of different fluids from sticking to the metasurface. A clear liquid phase interface is found in the images, as the two types of liquid used here do not mix (Supplementary Video 1). This gives rise to a square-function-shaped modulation (Fig. 4c). We note that a sinusoidal-function-like modulation is also possible by utilizing low-index cleaner dissolvable in high-index oil (Supplementary Fig. 5 and Supplementary Video 2). The designed dynamic meta-lens has a bulk refractive-index sensitivity of 37 nm per refractive index unit ($\mathrm{RIU}^{-1}$) and a figure of merit of 1.91 $\mathrm{RIU}^{-1}$. We note that our design is optimal for image-based spectrometer-less refractive-index sensing. The refractive-index information is decoded to the intensity of a bright focal spot, which allows low ISO sensing to obtain a larger dynamic range. Considering that the intensity of the focal point is modulated by ~300% with an ~30% refractive-index change under a light-emitting-diode-like illumination (Fig. 4c), the dynamic meta-lens shows great potential as an ultracompact refractive-index sensor in real-time chemical/biological sensing (Supplementary Fig. 6).

Finally, we demonstrate dynamic, integrated meta-optofluidics display functions. By leveraging mature microfluidics valve technology[44], we design and fabricate a transparent-metasurface digital number display (Fig. 4d). The display is composed of seven metasurface bars whose reflectivity can be individually controlled with a set of valves that can deliver either oil or air to the metasurface regions. Figure 4e shows the optical image of the integrated system, where polydimethylsiloxane microfluidic circuits (Supplementary Fig. 7) are stacked on top of the metasurface display elements that are patterned into a Si-on-sapphire wafer. An objective lens underneath the transparent sapphire wafer is used to illuminate and collect the reflected light from the display. Figure 4f shows the reflection images captured from the display, clearly demonstrating all the different digital numbers from 0 to 9 (Supplementary Video 3). The observed contrast ratio largely matches the performance of liquid-crystal displays without the use of polarizers, thereby paving a promising new way to the realization of metasurface displays on a transparent substrate.

## Conclusions

In conclusion, we have demonstrated a comprehensive dynamic-metasurface flat-optics platform that offers dynamic intensity and spectral control of light fields. The unprecedented high-spatial resolution and transparency provide new degrees of freedom in designing multifunctional, integrated and dynamic flat optics. The high sensitivity of scattering that is engineered into the metasurface elements also opens new sensing modalities by displaying subtle index changes in microfluidic channels. Combined with well-established large-scale microfluidic integration, this platform offers a bright future for dynamic display, imaging, holography and sensing applications.

## Online content

Any methods, additional references, Nature Research reporting summaries, source data, extended data, supplementary information, acknowledgements, peer review information; details of author contributions and competing interests; and statements of data and code availability are available at https://doi.org/10.1038/s41565-022-01197-y.

Received: 10 September 2021; Accepted: 18 July 2022;

## References

1. Squires, T. M. & Quake, S. R. Microfluidics: fluid physics at the nanoliter scale. *Rev. Mod. Phys.* **77**, 977–1026 (2005).
2. Sackmann, E. K., Fulton, A. L. & Beebe, D. J. The present and future role of microfluidics in biomedical research. *Nature* **507**, 181–189 (2014).
3. Chin, C. D., Linder, V. & Sia, S. K. Commercialization of microfluidic point-of-care diagnostic devices. *Lab Chip* **12**, 2118–2134 (2012).
4. Günther, A. & Jensen, K. F. Multiphase microfluidics: from flow characteristics to chemical and materials synthesis. *Lab Chip* **6**, 1487–1503 (2006).
5. Psaltis, D., Quake, S. R. & Yang, C. Developing optofluidic technology through the fusion of microfluidics and optics. *Nature* **442**, 381–386 (2006).
6. Monat, C., Domachuk, P. & Eggleton, B. J. Integrated optofluidics: a new river of light. *Nat. Photon.* **1**, 106–114 (2007).
7. Schmidt, H. & Hawkins, A. R. The photonic integration of non-solid media using optofluidics. *Nat. Photon.* **5**, 598–604 (2011).
8. Song, C. & Tan, S. H. A perspective on the rise of optofluidics and the future. *Micromachines* **8**, 152 (2017).
9. Genevet, P., Capasso, F., Aieta, F., Khorasaninejad, M. & Devlin, R. Recent advances in planar optics: from plasmonic to dielectric metasurfaces. *Optica* **4**, 139–152 (2017).
10. Wu, P. C. et al. Broadband wide-angle multifunctional polarization converter via liquid-metal-based metasurface. *Adv. Opt. Mater.* **5**, 1600938 (2017).
11. Zhang, W. et al. Microfluid-based soft metasurface for tunable optical activity in THz wave. *Opt. Express* **29**, 8786–8795 (2021).
12. Tokuda, Y., Iwasaki, S., Sato, Y., Nakanishi, Y. & Koike, H. Ubiquitous display for dynamically changing environments. In *CHI '03 Extended Abstracts on Human Factors in Computing Systems* 976–977 (ACM, 2003).
13. Chen, H. W., Lee, J. H., Lin, B. Y., Chen, S. & Wu, S. T. Liquid crystal display and organic light-emitting diode display: present status and future perspectives. *Light Sci. Appl.* **7**, 17168 (2018).
14. Comiskey, B., Albert, J. D., Yoshizawa, H. & Jacobson, J. J. An electrophoretic ink for all-printed reflective electronic displays. *Nature* **394**, 253–255 (1998).
15. Hayes, R. A. & Feenstra, B. J. Video-speed electronic paper based on electrowetting. *Nature* **425**, 383–385 (2003).
16. Heikenfeld, J. et al. Electrofluidic displays using Young–Laplace transposition of brilliant pigment dispersions. *Nat. Photon.* **3**, 292–296 (2009).
17. Feenstra, B. J. et al. A video-speed reflective display based on electrowetting: principle and properties. *J. Soc. Inf. Disp.* **12**, 293–299 (2004).
18. Cao, L., Fan, P., Barnard, E. S., Brown, A. M. & Brongersma, M. L. Tuning the color of silicon nanostructures. *Nano Lett.* **10**, 2649–2654 (2010).
19. Neder, V., Luxembourg, S. L. & Polman, A. Efficient colored silicon solar modules using integrated resonant dielectric nanoscatterers. *Appl. Phys. Lett.* **111**, 073902 (2017).

20. Yang, W. et al. All-dielectric metasurface for high-performance structural color. *Nat. Commun.* **11**, 1864 (2020).
21. Kristensen, A. et al. Plasmonic colour generation. *Nat. Rev. Mater.* **2**, 16088 (2016).
22. Huo, P. et al. Photorealistic full-color nanopainting enabled by a low-loss metasurface. *Optica* **7**, 1171–1172 (2020).
23. Lin, R. J. et al. Achromatic metalens array for full-colour light-field imaging. *Nat. Nanotechnol.* **14**, 227–231 (2019).
24. Holsteen, A. L., Lin, D., Kauvar, I., Wetzstein, G. & Brongersma, M. L. A light-field metasurface for high-resolution single-particle tracking. *Nano Lett.* **19**, 2267–2271 (2019).
25. Engheta, N., Salandrino, A. & Alù, A. Circuit elements at optical frequencies: nanoinductors, nanocapacitors, and nanoresistors. *Phys. Rev. Lett.* **95**, 95504 (2005).
26. Joo, W. et al. Metasurface-driven OLED displays beyond 10,000 pixels per inch. *Science* **370**, 459–463 (2020).
27. Sun, S. et al. Real-time tunable colors from micro fluidic reconfigurable all-dielectric metasurfaces. *ACS Nano* **12**, 2151–2159 (2018).
28. Komar, A. et al. Electrically tunable all-dielectric optical metasurfaces based on liquid crystals. *Appl. Phys. Lett.* **110**, 071109 (2017).
29. Zou, C. et al. Electrically tunable transparent displays for visible light based on dielectric metasurfaces. *ACS Photon.* **6**, 1533–1540 (2019).
30. Li, S.-Q. et al. Phase-only transmissive spatial light modulator based on tunable dielectric metasurface. *Science* **364**, 1087–1090 (2019).
31. Komar, A. et al. Dynamic beam switching by liquid crystal tunable dielectric metasurfaces. *ACS Photon.* **5**, 1742–1748 (2018).
32. Bomzon, Z., Biener, G., Kleiner, V. & Hasman, E. Space-variant Pancharatnam–Berry phase optical elements with computer-generated subwavelength gratings. *Opt. Lett.* **27**, 1141–1143 (2002).
33. Kerker, M., Wang, D. & Giles, C. L. Electromagnetic scattering by magnetic spheres. *J. Opt. Soc. Am.* **73**, 765–767 (1983).
34. Person, S. et al. Demonstration of zero optical backscattering from single nanoparticles. *Nano Lett.* **13**, 1806–1809 (2013).
35. Liu, W. & Kivshar, Y. S. Generalized Kerker effects in nanophotonics and meta-optics [Invited]. *Opt. Express* **26**, 13085–13105 (2018).
36. Pfeiffer, C. & Grbic, A. Metamaterial Huygens' surfaces: tailoring wave fronts with reflectionless sheets. *Phys. Rev. Lett.* **110**, 197401 (2013).
37. Decker, M. et al. High-efficiency dielectric Huygens' surfaces. *Adv. Opt. Mater.* **3**, 813–820 (2015).
38. Yu, Y. F. et al. High-transmission dielectric metasurface with 2π phase control at visible wavelengths. *Laser Photon. Rev.* **9**, 412–418 (2015).
39. Sauvan, C., Hugonin, J. P., Maksymov, I. S. & Lalanne, P. Theory of the spontaneous optical emission of nanosize photonic and plasmon resonators. *Phys. Rev. Lett.* **110**, 237401 (2013).
40. Auguié, B. & Barnes, W. L. Collective resonances in gold nanoparticle arrays. *Phys. Rev. Lett.* **101**, 143902 (2008).
41. Lin, D., Fan, P., Hasman, E. & Brongersma, M. L. Dielectric gradient metasurface optical elements. *Science* **345**, 298–302 (2014).
42. Bhushan, B., Hansford, D. & Lee, K. K. Surface modification of silicon and polydimethylsiloxane surfaces with vapor-phase-deposited ultrathin fluorosilane films for biomedical nanodevices. *J. Vac. Sci. Technol. A* **24**, 1197 (2006).
43. Mahadik, D. B. et al. Effect of concentration of trimethylchlorosilane (TMCS) and hexamethyldisilazane (HMDZ) silylating agents on surface free energy of silica aerogels. *J. Colloid Interface Sci.* **356**, 298–302 (2011).
44. Thorsen, T. Microfluidic large-scale integration. *Science* **298**, 580–584 (2002).

## Methods

**Numerical simulations.** We perform three-dimensional finite-element simulations in the frequency domain using the commercial software package COMSOL Multiphysics to study the optical properties of Si metasurfaces embedded in different dielectric environments (refractive index of the surrounding medium $n = 1.0$–$1.7$). In the full-field simulations (Fig. 3d and Supplementary Figs. 1 and 2), we apply periodic boundary conditions and use two ports along the light propagation direction to simulate the properties of Si nanoresonator arrays. In the quasi-normal-mode simulations (Fig. 2a and Supplementary Figs. 3 and 4), the two ports are replaced by perfect matching layers. We first study the case where Si nanoresonators are suspended in an isotropic dielectric environment without a substrate. Different types of Si are used in the simulation to match the specific experimental condition (single-crystalline Si for nanodisk array metasurfaces and poly-Si for geometric phase metasurfaces). The optical constants are retrieved from spectroscopic ellipsometry. We characterize the reflection and transmission of the Si nanoresonator array for a normally incident plane wave. The electric-field distribution inside the Si nanoresonator is extracted, too, and used for the multipole decomposition analysis. We also study the impact of the substrate underneath the metasurface. The refractive index of sapphire and fused silica is set as 1.77 and 1.46, respectively.

**Device fabrication.** *Si metasurfaces for dynamic reflectivity and colour control.* We start the fabrication with a 1 cm square 500-nm-thick single-crystalline Si on a sapphire substrate (MTI). Reactive ion etching (Lampoly) is used to thin down the Si film to 75 nm. Furthermore, 70-nm-thick hydrogen silsesquioxane (HSQ) is then spin coated on the Si film (4% HSQ, 4,000 rpm for 40 s) to serve as a negative-tone electron-beam resist layer followed by post-baking at 90 °C for 45 min. A thin conductive polymer layer (Espacer 300Z) is then spin coated on the Si film to mitigate charging effects during the electron-beam lithography process (JEOL 6300 100 kV system). The nominal electron-beam dose is set to ~2,000 $\mu\mathrm{C\,cm}^{-2}$ and the development is performed in 25% tetramethylammonium hydroxide for 2 min. Reactive ion etching is then used again to transfer the HSQ hard-mask patterns to the silicon slab, and the remaining HSQ hard-mask pattern is removed by immersing the sample in diluted 2% hydrogen fluoride solution for 1 min.

*Si geometric phase metasurfaces for dynamic diffraction efficiency and spectral control of phased-array optics.* We choose fused silica as the substrate for the geometric phase metasurfaces, since its isotropic refractive index is preferred over birefringent sapphire when modulated light transmits through the substrate. We first deposit a 200-nm-thick poly-Si layer on a fused silica substrate by low-pressure chemical vapour deposition. We note here that, in principle, single-crystalline Si can also be bonded to a borosilicate glass substrate by a more complex yet robust wafer-bonding process[45]. The optical constants and thickness of the poly-Si slab are measured by ellipsometry (J.A. Woollam M2000). The poly-Si slab is then etched down to 120 nm. The same fabrication process described above is subsequently conducted to pattern the poly-Si slab into metasurfaces.

*Microfluidic device fabrication and operation.* Devices are fabricated in polydimethylsiloxane (RTV 615, Momentive Performance Materials) by multilayer soft lithography. Each device consists of a two-layer elastomeric structure with a top control layer of channels that act as valves capable of pushing down and pinching off the channels to close them in the underlying liquid flow layer. This flow layer rests on the sample substrate, with the channels for injecting fluids (or air) overlaying the patterned display features.

Planar silicon moulds are defined by photolithography, using photomasks designed with computer-aided design software (AutoCAD, Autodesk) and printed on transparency films at a resolution of 20,000 dots per inch (FineLine Imaging). The moulds are fabricated on four-inch test-grade silicon wafers (University Wafer). The 'control' mould is fabricated using SU-8 2025 photoresist (Microchem) to deposit valve channels that are 24 µm in height. The 'flow' mould is fabricated with three lithographic steps. First, a blank layer of SU-8 2005 is deposited to promote the adhesion of subsequent layers. Next, areas that will be pinched off to restrict flow via the pressurization of the control channels are fabricated using 13-µm-high SPR220-7 photoresist (Shipley). These SPR220-7 channels are rounded to facilitate valve closure by incubation at 115 °C for 15 min. A hard bake at 190 °C for 2 h is used to prevent SPR photoresist erosion during the addition of subsequent layers. Finally, flow-channel features that will not be valved are fabricated using 14 µm SU-8 2015 photoresist (Microchem). All the photoresist processing is performed according to manufacturer specifications.

Oil, solvents and air are injected into the device via Tygon tubing and pins (New England Small Tube) by using pressure-driven flow from regulated house air. Valve actuation within the device is accomplished by applying pressure to water within the control channels, which deflects the polydimethylsiloxane membrane and pinches close the flow channel below. This turning on and off of pressure is controlled by pneumatic solenoid valves (Festo) driven by an ethernet-based, programmable field-bus input/output system with digital output modules (750-841 programmable field-bus controller and 750-504 four-channel digital output module; Wago). An open-source custom software platform written in Python 2.7 (ref. [46]) allows for real-time control and script-driven automation of all the aspects of the chip operation.

**Optical measurements.** *Sample dielectric environment setup.* A set of refractive-index liquids (Cargille Labs, $n = 1.4$–$1.7$) is used to set up the dielectric environment of the sample. A droplet of refractive-index liquids is transferred onto the sample by a pipettor and then covered by a microscopy cover glass before optical characterization (Supplementary Fig. 8a).

*Bright-field reflection measurements.* We perform the optical reflection measurement using a Nikon C2 confocal microscope (Supplementary Fig. 8b). Unpolarized light from a halogen lamp is used for top-illumination of the sample through a ×20 objective (Nikon, NA = 0.4). The reflection signal is then collected by the same objective and the reflection optical images of the samples are taken by a Nikon DS-Fi1 camera. A confocal scanner with a 60 µm pinhole is used to spatially select the signal, which is analysed using a SpectraPro 2300i spectrometer (150 lines per millimetre, blazed at $\lambda = 500$ nm) and Pixis Si charge-coupled device (−70 °C detector temperature). The reported spectra are averaged by 20 frames (1 s integration time each). All the reflection spectra are normalized by the reflection spectra of a protected silver mirror (Thorlabs, PF10-03-P01).

*Meta-lens characterization.* We characterize the focal point of the meta-lens using a Nikon C2 confocal microscope (Supplementary Fig. 8c). A monochromatic beam (bandwidth, ~5 nm) is generated first by an NKT SuperK EXTREME supercontinuum laser with an acousto-optic tunable filter. The beam is collimated and then circularly polarized using a linear polarizer followed by a quarter-wave plate. The meta-lens is bottom illuminated and its back focal plane (100 µm above the sample plane) is then imaged through a ×50 objective (NA = 0.6) and captured with a Nikon DS-Fi1 camera.

*Meta-hologram characterization.* We characterize the far-field distribution of the meta-hologram using a home-built optical setup (Supplementary Fig. 8d). The preparation of a collimated, circularly polarized monochromatic beam is described earlier. The sample is mounted on a three-axis translation stage and illuminated by the monochromatic beam weakly focused with a bulk lens ($f = 15$ cm). A whiteboard placed behind the translation stage is used as a projection screen, and images on the screen are finally captured by a Nikon D750 camera.

*Diffraction efficiency measurements.* To characterize the optical diffraction properties of the geometric phase metasurfaces, we construct a home-built angle-resolved spectroscopy setup (Supplementary Fig. 8e). A broadband beam from the supercontinuum source illuminates the metasurface at normal incidence and we characterize the first-order transmissivity. The metasurface sample and source are simultaneously rotated with respect to the collection optical path. Since the direction of the diffracted beams depends on the light frequency, we measure the diffracted radiant fluxes at different frequencies as we sweep the angle between the source and collection optical path. A 1-mm-wide pinhole (aperture stop) is located at the back focal plane of the collection lens to resolve the frequency component of the diffracted beam.

*Modulation with programmable microfluidics.* The microfluidic meta-lens is imaged using a custom Nikon Ti microscope with a transilluminator similar to the one described previously[47]. Light from a Lambda LS xenon arc lamp (Sutter) is passed through a band-pass filter (Semrock; centre wavelength, 565 nm; full-width at half-maximum, 24 nm) before being focused into a liquid light guide (Sutter). The other end of the liquid light guide is mounted above the sample by a custom three-dimensional printed assembly in place of the microscope condenser. Images are acquired with a scientific complementary metal–oxide–semiconductor camera (Andor) at 2 × 2 binning, using a ×20 objective (Nikon, NA = 0.45). The number display is imaged using the same Nikon Ti microscope, but using inverted microscopy with a ×2 objective (Nikon, NA = 0.1). Light is provided by a SOLA light engine (Lumencor) and filtered by standard fluorescence filter cubes (Semrock) mounted in a motorized filter turret. A 530 nm short-pass colour filter is inserted to enhance the contrast. The microscope is controlled by µManager software[48]. The images and videos are captured with a Nikon DS-Fi1 camera.

## Data availability

The data that support the plots within this paper and other findings of this study are available from the corresponding author upon reasonable request.

## References

45. Sell, D., Yang, J., Doshay, S., Zhang, K. & Fan, J. A. Visible light metasurfaces based on single-crystal silicon. *ACS Photon.* **3**, 1919–1925 (2016).
46. Longwell, S. AcqPack. *GitHub* https://github.com/FordyceLab/AcqPack (2017).
47. Gerver, R. E. et al. Programmable microfluidic synthesis of spectrally encoded microspheres. *Lab Chip* **12**, 4716–4723 (2012).

48. Edelstein, A. D. et al. Advanced methods of microscope control using μManager software. *J. Biol. Methods* **1**, e10 (2014).

## Acknowledgements

Q.L. thanks Z. Lyu for his help in the meta-hologram characterization. We acknowledge funding from AFOSR MURI grants (FA9550-17-1-0002 and FA9550-21-1-0312). P.M.F. is a Chan Zuckerberg Biohub Investigator.

## Author contributions

Q.L. and M.L.B. conceived the research idea. Q.L. built the analytical model and performed the design, fabrication and characterization of metasurfaces with input from J.v.d.G. J.-H.S. performed the poly-Si deposition and diffraction efficiency measurement. A.K.W. designed and fabricated the microfluidic cavities. S.A.L., A.K.W. and Q.L. conducted the microfluidic integration experiment. All the authors contributed to writing the manuscript. M.L.B. supervised the project.

## Competing interests

Q.L., J.v.d.G., J.-H.S. and M.L.B. are inventors on three US patent provisional applications (63/2711343, 63/2711350 and 63/2711354) held and submitted by Stanford University that cover the use of metasurface optofluidics for the dynamic control of light fields. The other authors declare no competing interests.

## Additional information

**Supplementary information** The online version contains supplementary material available at https://doi.org/10.1038/s41565-022-01197-y.

**Correspondence and requests for materials** should be addressed to Mark L. Brongersma.

**Peer review information** *Nature Nanotechnology* thanks Justus Ndukaife and the other, anonymous, reviewer(s) for their contribution to the peer review of this work.